AGU PUBLICATIONS

Geophysical Research Letters

RESEARCH LETTER
10.1002/2017GL074800

Key Points:
- Synthetic analysis suggests that the long-wavelength residual topography can be recovered from recent point-wise inferences in the ocean
- Appropriate damping factors must be used to recover the long-wavelength residual topography correctly
- Amplitude and pattern of the recovered long-wavelength residual topography from recent oceanic estimates agree with mantle flow predictions

Supporting Information:
- Supporting Information S1
- Data Set S1
- Data Set S2
- Data Set S3
- Data Set S4

Correspondence to:
T. Yang,
yang.t@unimelb.edu.au

Citation:
Yang, T., Moresi, L., Müller, R. D., & Gurnis, M. (2017). Oceanic residual topography agrees with mantle flow predictions at long wavelengths. *Geophysical Research Letters*, *44*, 10,896–10,906. https://doi.org/10.1002/2017GL074800

Received 5 JUL 2017
Accepted 17 OCT 2017
Accepted article online 24 OCT 2017
Published online 4 NOV 2017

Oceanic Residual Topography Agrees With Mantle Flow Predictions at Long Wavelengths

Ting Yang[1], Louis Moresi[1], R. Dietmar Müller[2], and Michael Gurnis[3]

[1]School of Earth Sciences, University of Melbourne, Melbourne, Victoria, Australia, [2]Earthbyte Group, School of Geosciences, University of Sydney, Sydney, New South Wales, Australia, [3]Seismological Laboratory, California Institute of Technology, Pasadena, CA, USA

Abstract Dynamic topography, the surface deflection induced by sublithosheric mantle flow, is an important prediction made by geodynamic models, but there is an apparent disparity between geodynamic model predictions and estimates of residual topography (total topography minus lithospheric and crustal contributions). We generate synthetic global topography fields with different power spectral slopes and spatial patterns to investigate how well the long-wavelength (spherical degrees 1 to 3) components can be recovered from a discrete set of samples where residual topography has been recently estimated. An analysis of synthetic topography, along with observed geoid and gravity anomalies, demonstrates the reliability of signal recovery. Appropriate damping factors, which depend on the maximum degree in the spherical harmonic expansion that is used to fit the samples, must be applied to recover the long-wavelength topography correctly; large damping factors smooth the model excessively and suppress residual topography amplitude and power spectra unrealistically. Recovered long-wavelength residual topographies based on recent oceanic point-wise estimates with different spherical expansion degrees agree with each other and with the predicted dynamic topography from mantle flow models. The peak amplitude of the long-wavelength residual topography from oceanic observations is about 1 km, suggesting an important influence of large-scale deep mantle flow.

1. Introduction

Mantle convection deflects the lithosphere and generates topography at the Earth's surface, which is generally referred to as *dynamic topography* (Parsons & Daly, 1983; Pekeris, 1935). Dynamic topography has an important influence on the gravitational field (Hager & Richards, 1989) and on long-term regional and global sea level trends (Gurnis, 1993; Lithgow-Bertelloni & Gurnis, 1997; Moucha et al., 2008; Spasojevic & Gurnis, 2012). It thus forms an important component of reconstructing continental surface environments through time and of understanding the driving forces behind associated transgressions and regressions of inland seas.

There are generally two means of estimating dynamic topography. One is to subtract contributions from the density heterogeneities within the crust and lithosphere (isostatic topography) from the total topography (Cochran & Talwani, 1977; Colin & Fleitout, 1990; Crough, 1978; Schroeder, 1984; Winterbourne et al., 2014). The derived dynamic topography using this approach is usually referred to as *residual topography*. Alternatively, surface deflections induced by mantle convection can be computed directly by solving the equations for viscous flow. The estimated large-scale dynamic topography based on these two strategies should be approximately consistent if the density and viscosity structures within the lithosphere and mantle are well constrained (Yang et al., 2016; Zhang et al., 2012). However, because isostatic topography from crustal and lithospheric loads dominates the total topography, and because the density and viscosity structures within the lithosphere and mantle are not well constrained (Le Stunff & Ricard, 1995; Panasyuk & Hager, 2000b), the estimated residual topography and calculated dynamic topography often do not agree. Although mantle flow models often predict large-amplitude negative dynamic topography in east and southeast Asia (Flament et al., 2013; Lithgow-Bertelloni & Gurnis, 1997; Lithgow-Bertelloni & Richards, 1998; Ricard et al., 1993; Steinberger, 2007; Yang & Gurnis, 2016; Zahirovic et al., 2016; Zhang et al., 2012), residual topography has been estimated to be close to zero or positive in the same region (Flament et al., 2013; Kaban et al., 2004; Le Stunff & Ricard, 1995; Panasyuk & Hager, 2000b; Wheeler & White, 2000). The amplitude of the estimated long-wavelength residual topography generally ranges between 0 and 500 m (Kaban et al., 2004; Le Stunff & Ricard, 1995; Panasyuk & Hager, 2000b; Wheeler & White, 2000), although some have estimated the values to

be higher, up to about 1 km (Davies & Pribac, 1993; Gurnis et al., 2000). In contrast, mantle flow models, which reproduce the observed geoid or stratigraphic records of stable continental interiors, usually predict long-wavelength dynamic topography with an amplitude of about 1 to 2 km (Conrad & Husson, 2009; Flament et al., 2013; Lithgow-Bertelloni & Gurnis, 1997; Lithgow-Bertelloni & Richards, 1998; Ricard et al., 1993; Steinberger, 2007; Yang & Gurnis, 2016; Zhang et al., 2012).

Efforts have been made to reduce predicted topographic amplitudes from mantle flow models so as to fit both the estimated residual topography and geoid observations (Čadek & Fleitout, 2003; Panasyuk & Hager, 2000a; Steinberger, 2007). Panasyuk and Hager (2000a) suggest that inclusion of one or more low viscosity layers within the mantle transition zone, the amplitude of dynamic topography can be significantly reduced through strongly decoupling lithospheric deflections from deep mantle flow. Although they inferred radial mantle viscosity profiles by a joint fit of the geoid and residual topography and the fit to the geoid is good, the fit to the estimated residual topography is not, with a variance reduction on residual topography less than 7% (Panasyuk & Hager, 2000a). Čadek and Fleitout (2003) inverted for lateral viscosity variations within the upper 300 km of the mantle and predicted a small-amplitude dynamic topography with the calculated geoid fitting the observed. However, the pattern of the calculated dynamic topography by Čadek and Fleitout (2003) appears at odds with residual topography estimations. For example, their predicted highest topography is centered on Taiwan in East Asia, inconsistent with residual topography estimates (Hoggard et al., 2017; Kaban et al., 2004; Panasyuk & Hager, 2000b; Steinberger, 2007).

Dynamic topography is especially difficult to estimate on the continents, due to their structural complexity. In contrast, oceanic regions are tectonically simpler and thus have the potential of yielding more precise estimates of residual topography. Recent estimates of residual topography in the oceanic realm (Czarnota et al., 2013; Hoggard et al., 2016; Hoggard et al., 2017; Winterbourne et al., 2014) considered precise contributions from within the crust and lithosphere, including sedimentary layer thickness and density, crustal thickness, and empirical bathymetry-age relationship. These point-wise estimates of residual topography, although sparse and unevenly distributed, have a large-scale pattern and amplitude consistent with mantle flow model predictions (Yang & Gurnis, 2016). However, the extent to which these unevenly distributed point-wise measurements constrain the pattern and amplitude of long-wavelength residual topography remains a topic of discussion (Hoggard et al., 2017). Here we address this issue using a series of synthetic residual topography fields and demonstrate that with the published observation locations, the long-wavelength (degrees 1 to 3) residual topography can be well constrained.

2. Method

To investigate the ability of recovering the long-wavelength (degrees 1 to 3) residual topography based on observations at sparse, irregularly distributed points, we first generate random synthetic topography fields and estimate their long-wavelength components by fitting a specific set of discrete samplings with spherical harmonic expansions.

A synthetic topography is generated from a combination of spherical harmonics up to degree 40 (about 1,000 km wavelength). At wavelengths less than 1,000 km, regional isostasy due to elastic flexure gradually dominates the topography. The synthetic topography h, is represented as

$$h(\theta,\varphi)=\sum_{l=1}^{40}\sum_{m=0}^{l}(C_{lm}\cos\varphi+S_{lm}\sin\varphi)P_l^m(\cos\theta) \tag{1}$$

Here θ and φ are colatitude and longitude, respectively. P_l^m is a Schmidt seminormalized associated Legendre polynomial of degree l and order m. The spherical harmonic coefficients C_{lm} and S_{lm} are generated following uniform random distribution first, but then the amplitude of each degree $A(l)=\sqrt{\sum_{m=0}^{l}\left(C_{lm}^2+S_{lm}^2\right)}$ is forced to vary as

$$A(l) = \begin{cases} 300 & l = 1 \\ 1000 \times l^p & l > 1 \end{cases} \quad (2)$$

Both recent estimates of residual topography (Hoggard et al., 2016; Hoggard et al., 2017) and dynamic topography predictions (Yang & Gurnis, 2016) suggest that the amplitude of dynamic topography at degree 1 is much smaller than that at degree 2. The exponent p controls the slope of the power spectra. By increasing the exponent p, short-wavelength contributions increase.

We sample the synthetic topography at 2,297 points fixed at locations of the Hoggard et al. (2017) data set, with the sampled values deviated from a given synthetic topography by a Gaussian distributed random error. The standard error is 200 m, similar to the observation error estimated by Hoggard et al. (2017), but see more discussions on the measurement error in the supporting information. Among the 2,297 points, 1,161 points are better constrained (Hoggard et al., 2017), and thus, the Gaussian distributed measurement error is halved. We then carry out spherical harmonic expansions based on these point-wise synthetic topography observations with the least squares method (Hoggard et al., 2016; Yang & Gurnis, 2016). To suppress unrealistic short-wavelength perturbations and to avoid over fitting the data, some form of damping is often used (for a general description of such problems in geophysics see (Hartzell & Heaton, 1983; Rawlinson & Sambridge, 2003; Tarantola, 2005)). A nonnegative damping factor λ_2, which mainly suppresses the spatial gradient of the function, is employed (Hartzell & Heaton, 1983) in most of our synthetic tests—see the supporting information for additional discussion. The long-wavelength components can be well recovered by choosing appropriate λ_2.

The power spectrum of the recovered spherical-harmonic expansion is compared against the prescribed synthetic topography power spectrum. The power spectrum at each degree is defined as the square of the amplitude:

$$P(l) = \sum_{m=0}^{l} \left(C_{lm}^2 + S_{lm}^2\right) \quad (3)$$

We define a variance difference to depict the power spectra difference between the synthetic and recovered topographies at long wavelengths (degrees 1 to 3). The variance difference is defined as

$$V_{1-3} = \frac{\sum_{l=1}^{3}\sum_{m=0}^{l}\left[\left(C_{lm}^R - C_{lm}^S\right)^2 + \left(S_{lm}^R - S_{lm}^S\right)^2\right]}{\sum_{l=1}^{3}\sum_{m=0}^{l}\left[\left(C_{lm}^S\right)^2 + \left(S_{lm}^S\right)^2\right]} \quad (4)$$

where S and R represent coefficients of the synthetic and recovered topographies, respectively. Long-wavelength components are well recovered for a small variance difference.

3. Results

We start with the long-wavelength (degrees 1–3) component recovery from a specific set of point-wise measurements of the synthetic topography. The synthetic topography has an exponent of $p = -0.3$, which generates substantial short-wavelength perturbations (Figure 1a) compared to long wavelengths (Figure 1b). For the same synthetic topography field, we conduct spherical harmonic expansions with different maximum expansion degrees and damping factors λ_2, while evaluating the error of the fit (Figures 1c–1f). The error of the fit to observations decreases with increasing maximum expansion degrees or number of inversion parameters (Figure 1c). The number of inversion parameters is $(l+1)^2$ for an expansion with the maximum degree l. However, beyond degrees about 5, the improvement in the misfit decreases slowly, especially when we consider the number of free parameters. In contrast to the error of the fit to observations, the average global difference between synthetic and recovered topographies *does not decrease* with increasing maximum expansion degree after 5 (Figure 1d). This is also true for the global long-wavelength topography difference (Figure 1e) and variance difference (Figure 1f). That the global synthetic-recovered topography differences do not decrease with increasing degrees beyond degree 5 indicates that the topography recoverability and resolution are constrained by the number and distribution of observations, and given the present topography observations, increasing the maximum spherical degree from degree 5 (36 parameters) to

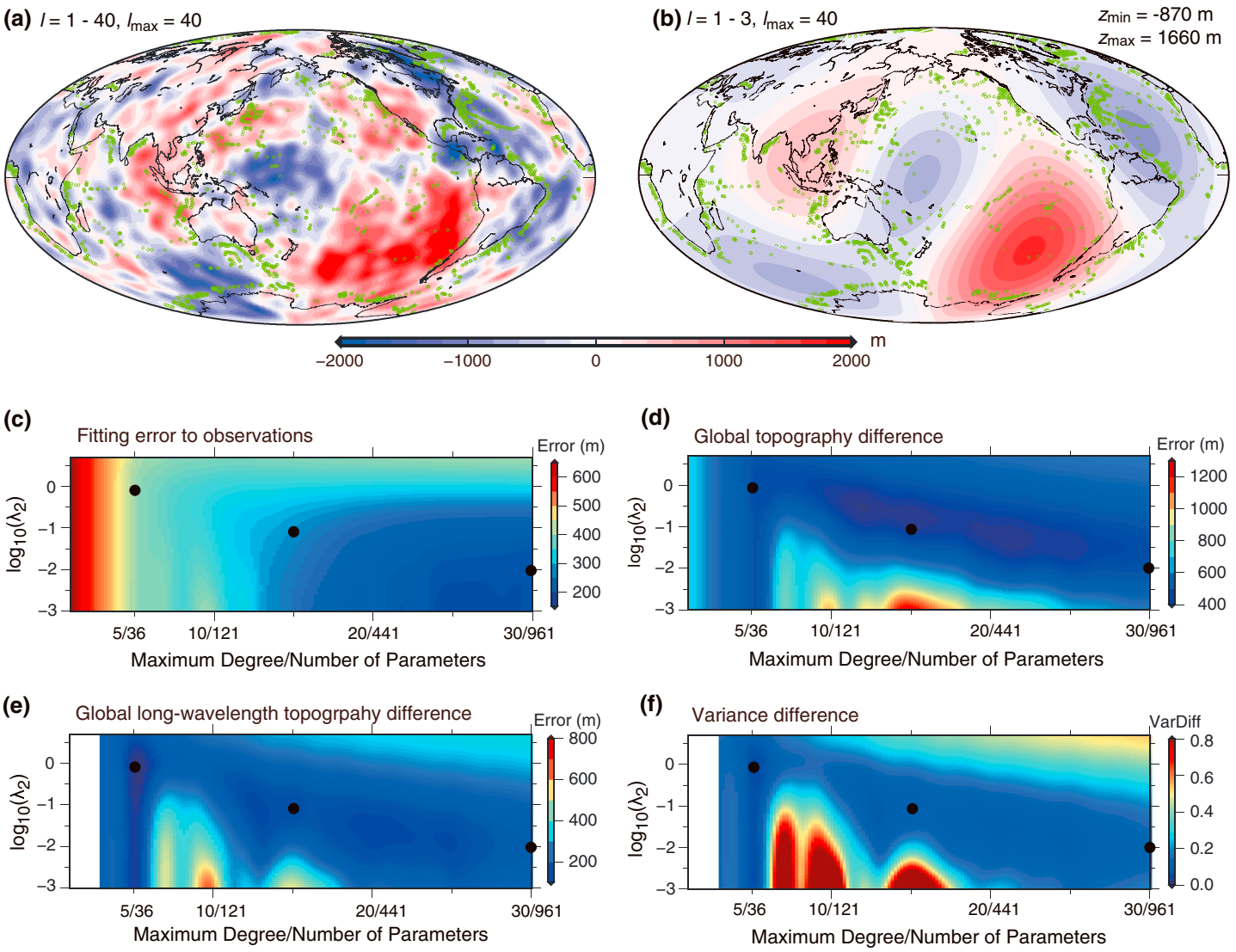

Figure 1. (a) Synthetic topography field represented by spherical harmonics up to degree 40 and its (b) long-wavelength (degrees 1–3) components. The green points represent the 2,297 point-wise observations whose values are assumed known. Locations of these observations follow Hoggard et al. (2017). The following quantities are shown as a function of maximum expanded spherical degrees and damping factors: (c) error of the fit to observations, (d) average difference between recovered and synthetic topographies across the globe, (e) average difference between recovered and synthetic long-wavelength topographies across the globe, and (f) variance difference. The black dots in Figures 1c–1f correspond to the appropriate damping factors chosen from the misfit-roughness relationships in Figures 2a–2c. The black dots in subsequent figures follow the same convention.

degree 30 (961 parameters) does not help resolving the global long-wavelength or short-wavelength features. Significantly, the error of the fit to observations and global synthetic-recovered topography differences is sensitive to the damping factor, when we truncate the expansion at a degree larger than about 5. With increasing number of degrees in the expansion, the appropriate damping factor decreases, suggesting that if more parameters are sought from the inversion, then one should not smooth the model excessively.

We fix the maximum expansion degrees to 5, 15, and 30, respectively, and investigate the influence of the damping factor on the error of the fit to observations and variance difference (Figures 2a–2c) in more detail. The model roughness, defined as the norm of the recovered topography gradient, is large when the model has large-amplitude short-wavelength perturbations. The roughness increases with the decrease of the damping factor. A smooth function has a large error of fit to observations, whereas a rough function usually yields a small error. A suitable compromise is often achieved at the elbow of the misfit-roughness plot (Deschamps et al., 2001; Hartzell & Heaton, 1983; Yue et al., 2013). With a maximum expansion degree 5 and the damping factor 0.84 that is chosen at the elbow of the misfit-roughness relationship, the

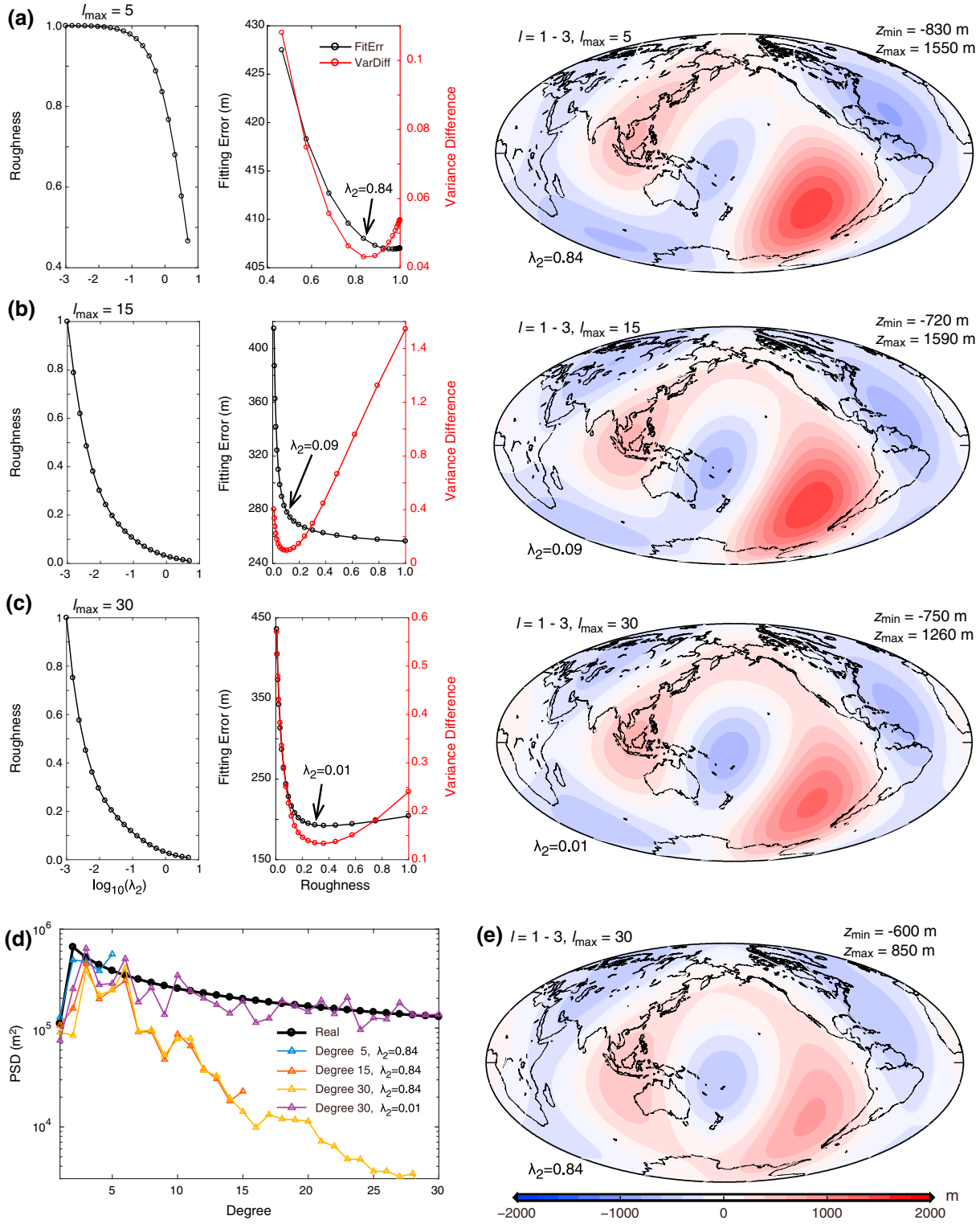

Figure 2. (a) Damping factor and recovered long-wavelength synthetic topography based on the misfit-roughness relationship with the maximum expansion degree fixed as 5. Left: Roughness of the recovered topography as a function of damping factor. Middle: error of the fit to observations (black) and variance difference (red) as a function of roughness. Right: The recovered long-wavelength (degrees 1–3) topography. The damping factor is chosen from the elbow of the misfit-roughness plot (black curve in the middle panel). (b and c) Same as Figure 2a but the maximum expansion degree is fixed as 15 (Figure 2b) and 30 (Figure 2c), respectively. (d) Power spectrum as a function of spherical degree with the damping factor fixed at 0.84 (Figure 1a). Different colors represent spherical expansions with different maximum degrees; green represents the synthetic. (e) Recovered long-wavelength topography with the maximum expansion degree as 30 and damping factor as 0.84.

predicted long-wavelength topography (Figure 2a) is comparable with the synthetic one (Figure 1b), in both pattern and amplitude. A slight change of the damping factor does not change the global topography differences (Figures 1d and 1e) or variance difference (Figures 1f and 2a) significantly. Good estimates of the long-wavelength topography are also found by fixing the maximum expansion degrees to 15 and 30, respectively, but with smaller damping factors (Figures 2b and 2c). Fixing the damping factor at 0.84 (elbow of the misfit-roughness relationship in Figure 2a), the recovered power spectra with different maximum expansions are compared against the synthesis (Figure 2d). Although the recovered power spectra are close to the actual values when the maximum expansion degree is around 5, they are strongly underestimated when the expansion grows to degree 30, with the peak-to-peak amplitude significantly suppressed (Figure 2e).

We generate additional random synthetic topography fields that also have the exponent $p = -0.3$ but differ significantly in spatial patterns with each other (Figure S1 in the supporting information). The long-wavelength components of these randomly generated synthetic topographies, can all be recovered, suggesting that the distribution of observations relative to the spatial pattern of topography has only limited influences on the long-wavelength components recovery.

Because the amplitude spectrum of the Earth's dynamic topography is unknown, we evaluate the robustness of synthetic topography recovery in terms of different amplitude spectra. Increasing the exponent p from -0.3 (Figure 1) to 0.0 significantly increases the short-wavelength synthetic topography contributions (Figure 3a) while reducing the exponent p from -0.3 to -0.8 significantly reduces the short-wavelength contributions (Figure 3f). Although increasing the maximum spherical degree beyond degree about 5 reduces the error of the fit to observations, it does not lead to a better recovery of the long-wavelength synthetic topography (Figures 3c and 3h). With appropriate damping factors chosen at the elbow of the misfit-roughness plot (Figures 3d and 3i), the recovered long-wavelength topographies (Figures 3e and 3j) are consistent with those of the synthetic topographies (Figures 3b and 3g).

Although increasing the maximum expansion degree after degree about 5 does not help reducing global synthetic-recovered topography differences, the magnitude of the power spectrum is largely reproduced when appropriate damping factors are chosen (Figures S2 and S3). However, the uncertainty is large and increases with increasing maximum expansion degrees. When large damping factors are used, the magnitude of the recovered power spectra is unrealistically suppressed (Figure S2). The spectral magnitude is strongly over estimated at short wavelengths when the short-wavelength energy is small (Figure S3f), especially for large measurement errors, possibly due to the over-fitting of the observations.

We explore the recovery of long-wavelength geoid and free-air gravity anomalies given the specific set of discrete observations. This is a helpful set of experiments as the geoid, gravity anomalies, and dynamic topography are closely related (Hager et al., 1984; Yang & Gurnis, 2016) and synthetic topography generally has a different long-wavelength phase and power spectrum from either the geoid or the dynamic topography. The geoid is dominated by long-wavelength components (Figures S4a and S4b), while the free-air gravity anomaly has substantial short-wavelength contributions (Figures S4e and S4f). Our tests suggest that we are able to recover the long-wavelength components of these fields (Figures S4d and S4h), strengthening the argument that long-wavelength residual topography can be recovered from the sparse estimates by Hoggard et al. (2017).

We recover the long-wavelength dynamic topography based on recent point-wise residual topography estimates in the oceanic realm (Hoggard et al., 2017) and compare them with mantle flow predictions (Yang & Gurnis, 2016). Residual topography estimates show a good correlation with the predicted dynamic topography from mantle flow models (Figures 4a and 4b). For example, mantle flow models predict large-scale uplift in the central Pacific and around southern Africa, matching large positive residual topography. Mantle flow models predict large depressions around subducted slabs, where the residual topography is also low. We carry out spherical harmonic expansions of the 2297 residual topography observations from Hoggard et al. (2017) with different maximum expansion degrees and damping factors (Figure 4c). With the maximum spherical degrees as 5, 12, and 30, we set the corresponding damping factors to 0.55, 0. 057, and 0.01, respectively, based on the misfit-roughness relationship (Figure S5). The estimated long-wavelength (degree 1 to 3) residual topography with different expansion degrees yields similar spatial patterns and amplitudes (Figures 4d–4f) and agrees with mantle flow model predictions (Figure 4b). The estimated long-wavelength residual topography has a peak-to-peak amplitude of 1 km (Figures 4d–4f), contrary to the results of Hoggard

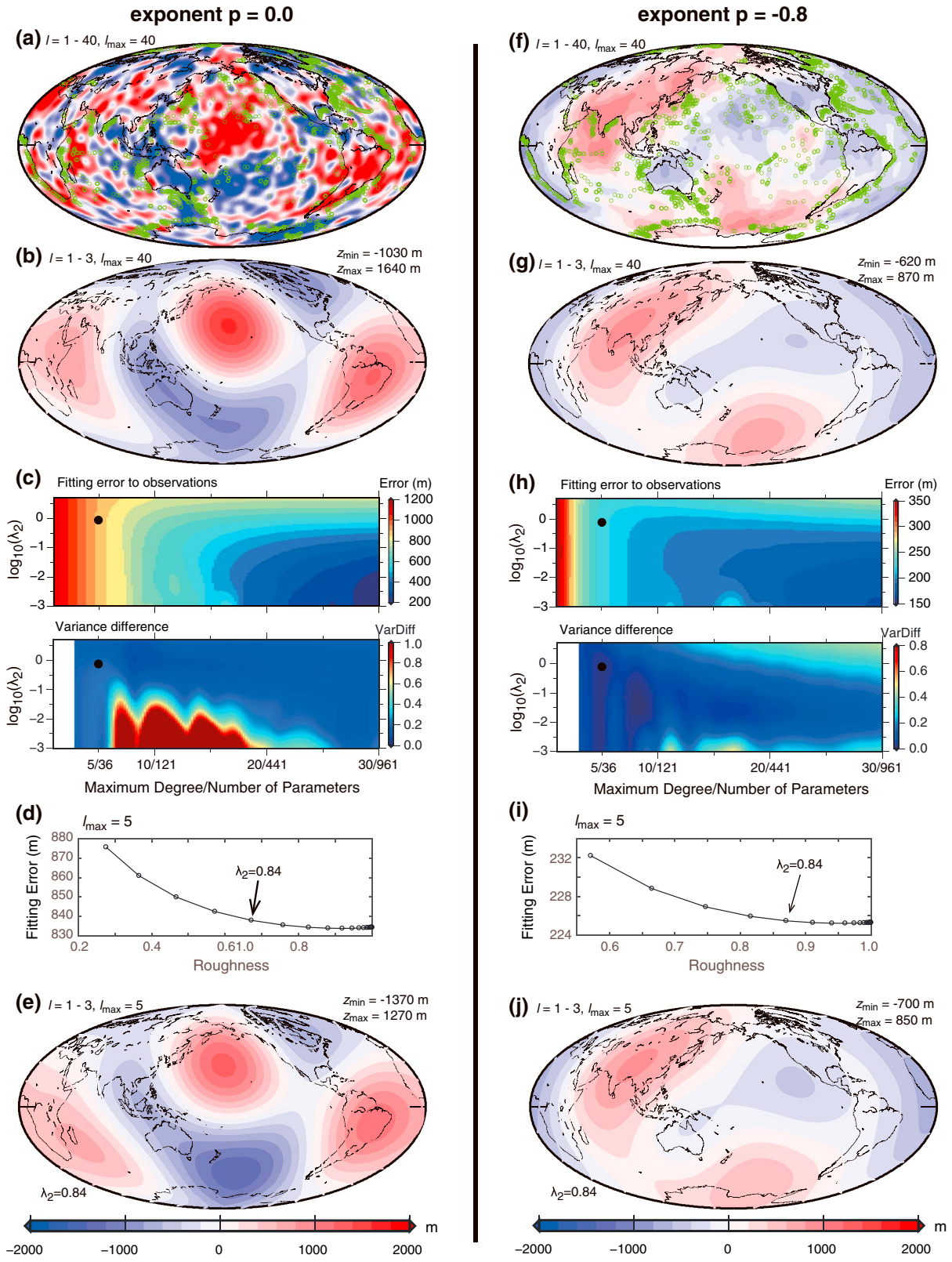

Figure 3. Long-wavelength topography recovery for synthetic models with different power spectra. (a–e) Spectral power does not decrease with increasing degree (exponent $p = 0.0$). (f–j) Spectral power decreases faster with increasing degrees as compared with the case in Figure 1 (exponent $p = -0.8$). Synthetic topography (Figures 3a and 3f), their long-wavelength components (Figures 3b and 3g), error of the fit to observations and variance difference (Figures 3c and 3h), damping factor from misfit-roughness plot (Figures 3d and 3i), and the recovered long-wavelength topographies (Figures 3e and 3j) are presented.

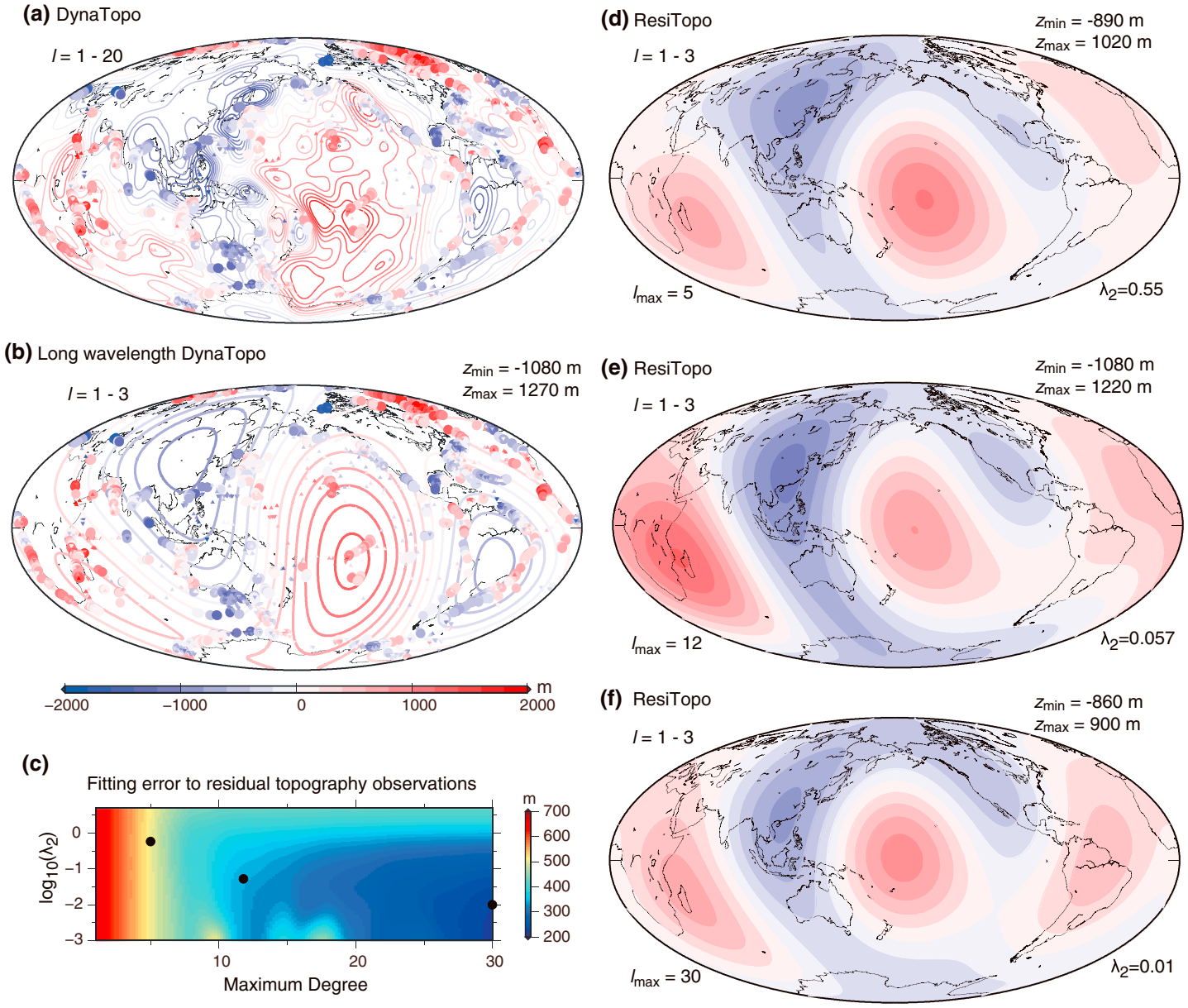

Figure 4. Comparisons between mantle flow model predicted dynamic topography and recent estimated residual topography in the oceanic realm. (a) Dynamic topography and (b) its long-wavelength (degrees 1–3) components are from Yang and Gurnis (2016). (c) Error of the fit to 2297 residual topography observations. (d–f) Inferred long-wavelength residual topography based on 2,297 observations with the maximum expansion degrees as 5, 12, and 30. The corresponding damping factor for each degree is chosen from the elbow of the misfit-roughness relationships (figure S5). In Figures 4a and 4b, the circles represent the 1,161 observations that have both precise sedimentary and crustal corrections, while the upward and downward pointing triangles represent the remaining points for which residual topography might be overestimated or underestimated, respectively (Hoggard et al., 2017).

et al. (2017), who used a combination of gradient regularization damping factor λ_2 and amplitude damping factor λ_1 that vary between 0.32 and 3.2 and between 100 and 1,000, respectively. Using these damping factors, amplitudes of the recovered dynamic topography are significantly smaller (Figure S6). The estimated residual topography power spectrum is compared with that of dynamic topography from mantle flow predictions (Figure S7). Due to the jagged perturbations of the recovered power spectrum around true values (Figures S2 and S3), only first-order features of the recovered power spectra are described. At degrees lower than ~15, spectral magnitudes of the estimated residual topography and dynamic topography are generally consistent. However, at degrees larger than ~15, residual topography spectral magnitude is significantly larger than that of dynamic topography. This inconsistency at short

wavelengths may originate from the limitation of mantle flow model predictions (see discussions in Yang & Gurnis, 2016) or from limitations in residual topography spectral estimates (Figure S3f). The residual topography spectral power of degrees larger than 15 is around one order smaller than that of degrees 2 and 3, suggesting a factor of 2 to 3 in amplitude reduction.

4. Discussion and Conclusion

Dynamic topography is an important prediction of mantle flow models. However, its amplitude and pattern are controversial. We conduct synthetic experiments and demonstrate that long-wavelength dynamic topography components can be recovered from recent point-wise residual topography observations in the oceanic realm (Hoggard et al., 2017). An analysis of the geoid and free-air gravity fields further consolidates this argument. Spherical expansions of recent residual topography observations with different maximum degrees and respective appropriate damping factors all yield large-amplitude long-wavelength residual topography that agrees with the mantle flow model predictions.

The prominent uplift around the central Pacific and southwest Indian Ocean and the depression around southeast Asia that have long been predicted by mantle flow models (Conrad & Husson, 2009; Flament et al., 2013; Gurnis, 1993; Hager & Richards, 1989; Lithgow-Bertelloni & Gurnis, 1997; Lithgow-Bertelloni & Richards, 1998; Ricard et al., 1993; Spasojevic & Gurnis, 2012; Steinberger, 2007; Yang & Gurnis, 2016; Zhang et al., 2012) are well revealed by the recovered long-wavelength residual topography (Figure 4). Many residual topography models, although with large uncertainties, suggest a large-scale negative dynamic topography around South America (Kaban et al., 2004; Panasyuk & Hager, 2000b; Steinberger, 2007). Point-wise residual topography observations also show a deep Argentine Basin (Figure 4a) that is consistent with mantle flow model predictions (Shephard et al., 2012). However, the amplitude of the negative long-wavelength dynamic topography around South America is small (Figure 4b), and shallow density heterogeneities may exert additional contributions regionally (Rodríguez Tribaldos et al., 2017), making the recovery of long-wavelength negative dynamic topography around South America more difficult.

Dynamic topography includes various wavelengths with contributions from sublithosphere instabilities, plumes, and other upper mantle heterogeneities potentially playing important roles in generating short-wavelength topography perturbations (Faccenna & Becker, 2010; Huang & Zhong, 2005; King & Ritsema, 2000; Robinson & Parsons, 1988; Schoonman et al., 2017; Yang & Leng, 2014). However, our synthetic experiments suggest that the topographic recoverability is constrained by the present distribution of residual topography observations. Although short-wavelength topographic perturbations may be recovered locally with dense data coverages, increasing the maximum spherical degree from about degree 5 to degree 30 does not help the recovery of shorter-wavelength features globally. On the other hand, the recovered residual topography power spectrum is generally consistent with that of dynamic topography for degrees less than 15. But the uncertainty is large and when the short-wavelength topographic relief is small while the measurement error is large, the spectral magnitude at short wavelengths may be strongly over estimated.

The choice of damping factors is important in parameter estimates, especially when the number of parameters inverted is large and the problem is underdetermined (Hartzell & Heaton, 1983; Rawlinson & Sambridge, 2003; Tarantola, 2005). Both the error of the fit to observations and global synthetic-recovered topography differences depend on the choice of damping factors critically when the maximum expansion degree is larger than about 5 in the synthetic models investigated. The appropriate damping factors have a decreasing trend with increasing maximum expansion degree, suggesting that if one wants to fit the observation with more parameters, one should not smooth the model excessively. The small-amplitude long-wavelength residual topography derived by Hoggard et al. (2016) and Hoggard et al. (2017) is due to the large damping factor used. Although the conclusion that the residual topography amplitude reaches ~ 1 km should not be influenced by a slight change of the damping factor, more objective ways may be needed in the future to yield the most appropriate maximum expansion degrees and damping factors automatically (Rawlinson & Sambridge, 2003). The influence of truncating spherical harmonic expansions to a certain degree on long-wavelength residual topography recovery may also need to be considered (Trampert & Snieder, 1996).

Acknowledgments
T.Y. benefitted from the discussion with Judith Sippel on residual topography. The authors thank Malcolm Sambridge and two anonymous reviewers for reading the original manuscript and providing insightful suggestions. M.G. has been supported by the National Science Foundation through EAR-1358646, EAR-1600956, and EAR-1645775 and by Statoil ASA. L.M. and R. D.M. were supported by Australian Research Council grants DP130101946 and IH130200012. Dynamic topography and the recovered long-wavelength residual topography data are listed in the supporting information.

References

Čadek, O., & Fleitout, L. (2003). Effect of lateral viscosity variations in the top 300 km on the geoid and dynamic topography. *Geophysical Journal International*, *152*(3), 566–580. https://doi.org/10.1046/j.1365-246X.2003.01859.x

Cochran, J. R., & Talwani, M. (1977). Free-air gravity anomalies in the world's oceans and their relationship to residual elevation. *Geophysical Journal International*, *50*(3), 495–552. https://doi.org/10.1111/j.1365-246X.1977.tb01334.x

Colin, P., & Fleitout, L. (1990). Topography of the ocean floor: Thermal evolution of the lithosphere and interaction of deep mantle heterogeneities with the lithosphere. *Geophysical Research Letters*, *17*, 1961–1964. https://doi.org/10.1029/GL017i011p01961

Conrad, C. P., & Husson, L. (2009). Influence of dynamic topography on sea level and its rate of change. *Lithosphere*, *1*(2), 110–120. https://doi.org/10.1130/L32.1

Crough, S. T. (1978). Thermal origin of mid-plate hot-spot swells. *Geophysical Journal International*, *55*(2), 451–469. https://doi.org/10.1111/j.1365-246X.1978.tb04282.x

Czarnota, K., Hoggard, M., White, N., & Winterbourne, J. (2013). Spatial and temporal patterns of Cenozoic dynamic topography around Australia. *Geochemistry, Geophysics, Geosystems*, *14*, 634–658. https://doi.org/10.1029/2012GC004392

Davies, G. F., & Pribac, F. (1993). Mesozoic seafloor subsidence and the Darwin Rise, past and present. In M. S. Pringle, et al. (Eds.), *The Mesozoic Pacific: Geology, tectonics, and volcanism*, (pp. 39–52). Washington, D. C: American Geophysical Union. https://doi.org/10.1029/GM077p0039

Deschamps, F., Snieder, R., & Trampert, J. (2001). The relative density-to-shear velocity scaling in the uppermost mantle. *Physics of the Earth and Planetary Interiors*, *124*(3-4), 193–212. https://doi.org/10.1016/S0031-9201(01)00199-6

Faccenna, C., & Becker, T. W. (2010). Shaping mobile belts by small-scale convection. *Nature*, *465*(7298), 602–605. https://doi.org/10.1038/nature09064

Flament, N., Gurnis, M., & Müller, R. D. (2013). A review of observations and models of dynamic topography. *Lithosphere*, *5*(2), 189–210. https://doi.org/10.1130/L245.1

Gurnis, M. (1993). Phanerozoic marine inundation of continents driven by dynamic topography above subducting slabs. *Nature*, *364*(6438), 589–593. https://doi.org/10.1038/364589a0

Gurnis, M., Mitrovica, J. X., Ritsema, J., & van Heijst, H. J. (2000). Constraining mantle density structure using geological evidence of surface uplift rates: The case of the African superplume. *Geochemistry, Geophysics, Geosystems*, *1*, 1020. https://doi.org/10.1029/1999GC000035

Hager, B. H., Clayton, R. W., Richards, M. A., Comer, R. P., & Dziewonski, A. M. (1984). Lower mantle heterogeneity, dynamic topography and the geoid. *Nature*, *313*, 541–545.

Hager, B., & Richards, M. (1989). Long-wavelength variations in Earth's geoid: Physical models and dynamical implications. *Philosophical Transactions of the Royal Society of London A: Mathematical, Physical and Engineering Sciences*, *328*(1599), 309–327. https://doi.org/10.1098/rsta.1989.0038

Hartzell, S. H., & Heaton, T. H. (1983). Inversion of strong ground motion and teleseismic waveform data for the fault rupture history of the 1979 Imperial Valley, California, earthquake. *Bulletin of the Seismological Society of America*, *73*(6A), 1553–1583.

Hoggard, M., White, N., & Al-Attar, D. (2016). Global dynamic topography observations reveal limited influence of large-scale mantle flow. *Nature Geoscience*, *9*(6), 456–463. https://doi.org/10.1038/ngeo2709

Hoggard, M. J., Winterbourne, J., Czarnota, K., & White, N. (2017). Oceanic residual depth measurements, the plate cooling model and global dynamic topography. *Journal of Geophysical Research: Solid Earth*, *122*, 2328–2372. https://doi.org/10.1002/2016JB013457

Huang, J., & Zhong, S. (2005). Sublithospheric small-scale convection and its implications for the residual topography at old ocean basins and the plate model. *Journal of Geophysical Research*, *110*, B05404. https://doi.org/10.1029/2004JB003153

Kaban, M., Schwintzer, P., & Reigber, C. (2004). A new isostatic model of the lithosphere and gravity field. *Journal of Geodesy*, *78*(6), 368–385. https://doi.org/10.1007/s00190-004-0401-6

King, S. D., & Ritsema, J. (2000). African hot spot volcanism: Small-scale convection in the upper mantle beneath cratons. *Science*, *290*(5494), 1137–1140. https://doi.org/10.1126/science.290.5494.1137

Le Stunff, Y., & Ricard, Y. (1995). Topography and geoid due to lithospheric mass anomalies. *Geophysical Journal International*, *122*(3), 982–990. https://doi.org/10.1111/j.1365-246X.1995.tb06850.x

Lithgow-Bertelloni, C., & Gurnis, M. (1997). Cenozoic subsidence and uplift of continents from time-varying dynamic topography. *Geology*, *25*(8), 735–738. https://doi.org/10.1130/0091-7613(1997)025%3C0735:CSAUOC%3E2.3.CO;2

Lithgow-Bertelloni, C., & Richards, M. A. (1998). The dynamics of Cenozoic and Mesozoic plate motions. *Reviews of Geophysics*, *36*, 27–78. https://doi.org/10.1029/97RG02282

Moucha, R., Forte, A. M., Mitrovica, J. X., Rowley, D. B., Quéré, S., Simmons, N. A., & Grand, S. P. (2008). Dynamic topography and long-term sea-level variations: There is no such thing as a stable continental platform. *Earth and Planetary Science Letters*, *271*(1-4), 101–108. https://doi.org/10.1016/j.epsl.2008.03.056

Panasyuk, S. V., & Hager, B. H. (2000a). Inversion for mantle viscosity profiles constrained by dynamic topography and the geoid, and their estimated errors. *Geophysical Journal International*, *143*(3), 821–836. https://doi.org/10.1046/j.0956-540X.2000.01286.x

Panasyuk, S. V., & Hager, B. H. (2000b). Models of isostatic and dynamic topography, geoid anomalies, and their uncertainties. *Journal of Geophysical Research*, *105*, 28,199–28,209. https://doi.org/10.1029/2000JB900249

Parsons, B., & Daly, S. (1983). The relationship between surface topography, gravity anomalies, and temperature structure of convection. *Journal of Geophysical Research*, *88*, 1129–1144. https://doi.org/10.1029/JB088iB02p01129

Pekeris, C. L. (1935). Thermal convection in the interior of the Earth. *Geophysical Journal International*, *3*(8), 343–367. https://doi.org/10.1111/j.1365-246X.1935.tb01742.x

Rawlinson, N., & Sambridge, M. (2003). Seismic traveltime tomography of the crust and lithosphere. *Advances in Geophysics*, *46*, 81–198. https://doi.org/10.1016/S0065-2687(03)46002-0

Ricard, Y., Richards, M., Lithgow-Bertelloni, C., & Le Stunff, Y. (1993). A geodynamic model of mantle density heterogeneity. *Journal of Geophysical Research*, *98*, 21,895–21,909. https://doi.org/10.1029/93JB02216

Robinson, E., & Parsons, B. (1988). Effect of a shallow low-viscosity zone on the formation of midplate swells. *Journal of Geophysical Research*, *93*, 3144–3156. https://doi.org/10.1029/JB093iB04p03144

Rodríguez Tribaldos, V., White, N. J., Roberts, G., & Hoggard, M. J. (2017). Spatial and Temporal Uplift History of South America from Calibrated Drainage Analysis. *Geochemistry, Geophysics, Geosystems*, *18*, 2321–2353.

Schoonman, C., White, N., & Pritchard, D. (2017). Radial viscous fingering of hot asthenosphere within the Icelandic plume beneath the North Atlantic Ocean. *Earth and Planetary Science Letters*, *468*, 51–61. https://doi.org/10.1016/j.epsl.2017.03.036

Schroeder, W. (1984). The empirical age-depth relation and depth anomalies in the Pacific Ocean Basin. *Journal of Geophysical Research*, *89*, 9873–9883. https://doi.org/10.1029/JB089iB12p09873

Shephard, G., Liu, L., Müller, R., & Gurnis, M. (2012). Dynamic topography and anomalously negative residual depth of the Argentine Basin. *Gondwana Research*, *22*(2), 658–663. https://doi.org/10.1016/j.gr.2011.12.005

Spasojevic, S., & Gurnis, M. (2012). Sea level and vertical motion of continents from dynamic Earth models since the Late Cretaceous. *AAPG Bulletin*, *96*(11), 2037–2064. https://doi.org/10.1306/03261211121

Steinberger, B. (2007). Effects of latent heat release at phase boundaries on flow in the Earth's mantle, phase boundary topography and dynamic topography at the Earth's surface. *Physics of the Earth and Planetary Interiors*, *164*(1-2), 2–20. https://doi.org/10.1016/j.pepi.2007.04.021

Tarantola, A. (2005). *Inverse problem theory and methods for model parameter estimation*. Philadelphia, PA: Society for Industrial and Applied Mathematics. https://doi.org/10.1137/1.9780898717921

Trampert, J., & Snieder, R. (1996). Model estimations biased by truncated expansions: Possible artifacts in seismic tomography. *Science*, *271*(5253), 1257–1260. https://doi.org/10.1126/science.271.5253.1257

Wheeler, P., & White, N. (2000). Quest for dynamic topography: Observations from Southeast Asia. *Geology*, *28*(11), 963–966. https://doi.org/10.1130/0091-7613(2000)28%3C963:QFDTOF%3E2.0.CO;2

Winterbourne, J., White, N., & Crosby, A. (2014). Accurate measurements of residual topography from the oceanic realm. *Tectonics*, *33*, 982–1015. https://doi.org/10.1002/2013TC003372

Yang, T., & Gurnis, M. (2016). Dynamic topography, gravity and the role of lateral viscosity variations from inversion of global mantle flow. *Geophysical Journal International*, *207*(2), 1186–1202. https://doi.org/10.1093/gji/ggw335

Yang, T., Gurnis, M., & Zahirovic, S. (2016). Slab avalanche-induced tectonics in self-consistent dynamic models. *Tectonophysics*. https://doi.org/10.1016/j.tecto.2016.12.007

Yang, T., & Leng, W. (2014). Dynamics of hidden hotspot tracks beneath the continental lithosphere. *Earth and Planetary Science Letters*, *401*, 294–300. https://doi.org/10.1016/j.epsl.2014.06.019

Yue, H., Lay, T., Freymueller, J. T., Ding, K., Rivera, L., Ruppert, N. A., & Koper, K. D. (2013). Supershear rupture of the 5 January 2013 Craig, Alaska (M_w 7.5) earthquake. *Journal of Geophysical Research: Solid Earth*, *118*, 5903–5919. https://doi.org/10.1002/2013JB010594

Zahirovic, S., Flament, N., Dietmar Müller, R., Seton, M., & Gurnis, M. (2016). Large fluctuations of shallow seas in low-lying Southeast Asia driven by mantle flow. *Geochemistry, Geophysics, Geosystems*, *17*, 3589–3607. https://doi.org/10.1002/2016GC006434

Zhang, N., Zhong, S., & Flowers, R. M. (2012). Predicting and testing continental vertical motion histories since the Paleozoic. *Earth and Planetary Science Letters*, *317*, 426–435.